Numerical Investigation of the Seismic Response of Trapezoidal Corrugated Web Steel Frame Structures

Huimin Cao[1,2,3,*], Xiaoliang Yao[1], Xuan Cui[2], Hui Lu[2], Yaping Xu[2] and Xin-e Yan[2,3]

[1] School of Civil Engineering and Architecture, Xi'an University of Technology, Xi'an, 710048, China

[2] School of Civil and Railway Engineering, Xi'an Traffic Engineering Institute, Xi'an, 710300, China

[3] Xi'an Key Laboratory of Monitoring and Prevention of Railway Roadbed Damage, Xi'an, 710000, China

Revista Internacional
Métodos numéricos
para cálculo y diseño en ingeniería
RIMNI
UNIVERSITAT POLITÈCNICA DE CATALUNYA BARCELONATECH
In cooperation with CIMNE

INFORMATION

Keywords:
Trapezoidal corrugated web
elasto-plastic time-history
seismic performance

DOI: 10.23967/j.rimni.2026.10.74634

SCIPEDIA Revista Internacional de Métodos Numéricos para Cálculo y Diseño en Ingeniería

Revista Internacional Métodos numéricos para cálculo y diseño en ingeniería RIMNI

In cooperation with CIMNE

Numerical Investigation of the Seismic Response of Trapezoidal Corrugated Web Steel Frame Structures

Huimin Cao[1,2,3,*], **Xiaoliang Yao**[1], **Xuan Cui**[2], **Hui Lu**[2], **Yaping Xu**[2] and **Xin-e Yan**[2,3]

[1]School of Civil Engineering and Architecture, Xi'an University of Technology, Xi'an, 710048, China

[2]School of Civil and Railway Engineering, Xi'an Traffic Engineering Institute, Xi'an, 710300, China

[3]Xi'an Key Laboratory of Monitoring and Prevention of Railway Roadbed Damage, Xi'an, 710000, China

ABSTRACT

Using the ABAQUS finite element analysis platform, this study established numerical models of H-section steel members with trapezoidal corrugated webs and a three-story corrugated web steel frame. The dynamic characteristics of the frame structure were investigated via modal analysis and elasto-plastic time-history analysis. Employing the control variable method, the study first determined the key structural parameters of the corrugated web steel frame: specifically, a web thickness of 2 mm, a corrugation angle of 45°, a wavelength of 240 mm, and a wave height of 30 mm. Subsequently, a three-story frame model was constructed based on these parameters, and the structure's seismic performance under the El Centro and Taft seismic waves was analyzed. The results demonstrate that the three-story corrugated web steel frame system exhibits excellent hysteretic energy dissipation capacity under low-cycle reversed loading. Structural deformation is dominated by lateral displacement, with the peak inter-story displacement reaching 3.76 times the longitudinal displacement. The second floor is identified as the structural weak link. Compared with the Taft wave, the El Centro wave exerts a more significant influence on the structure's dynamic response and induces more pronounced displacement and stress responses under the same seismic intensity.

OPEN ACCESS

Received: 15/10/2025

Accepted: 12/12/2025

Published: 20/03/2026

DOI
10.23967/j.rimni.2026.10.74634

Keywords:
Trapezoidal corrugated web
elasto-plastic time-history
seismic performance

1 Introduction

The trend towards long-span and lightweight structural systems has exposed limitations in traditional flat web steel members, primarily due to their pronounced susceptibility to buckling and considerable self-weight, which restrict their application in complex engineering scenarios [1,2]. In contrast, trapezoidal corrugated web steel structures provide a coordinated optimization by reducing self-weight by 20%–30% while increasing shear stiffness by over 40%, making them widely adopted in bridges and industrial buildings [3]. The dynamic characteristics and seismic performance of such structures are critical to structural safety and form the basis of rational design.

Considerable research has been conducted on the dynamic behavior of trapezoidal corrugated webs, though most studies focus on component-level performance [4]. For instance, Mao et al. [5]

*Correspondence: Huimin Cao (chuimin2024@163.com). This is an article distributed under the terms of the Creative Commons BY-NC-SA license

compared the dynamic responses of 30 m single-box single-cell and 50 m single-box multi-cell composite girders with corrugated steel webs against conventional concrete box girders, showing that corrugated web girders exhibit lower natural frequencies. Cao et al. [6] investigated the influence of corrugation angles on dynamic response, damage evolution, and impact resistance of composite structures, providing references for damage prediction and impact assessment. Li et al. [7] demonstrated via ABAQUS that horizontal corrugated steel plate shear walls exhibit superior hysteretic performance and energy dissipation under low-cycle reversed loading, which is advantageous for seismic resistance.

Recent component-level studies have further refined design guidance. Leblouba et al. [8] performed 18 shear tests on trapezoidal corrugated webs and proposed a normalized strength model that predicts ultimate shear capacity within ±5% of test data, giving designers a direct alternative to EN 1993-1-5. Zhou et al. [9] studied nonprismatic corrugated web beams, finding the "full shear-bearing web" hypothesis invalid—Resal effect drives redistribution, web buckling occurs away from supports, and concrete cracking impacts capacity. Qiao et al. [10] subjected full-scale corrugated steel-plate shear walls to cyclic loading under three boundary conditions; vertically oriented corrugations delivered 30% higher initial stiffness and 25% greater cumulative energy dissipation than flat plates, while the addition of discrete dampers postponed fracture by 15% drift cycles, offering a practical seismic upgrade for frame systems. Leblouba et al. [11] mapped shear-buckling and stress-concentration fields with 3-D DIC, identifying that the ratio of fold-width to corrugation-angle governs the transition from local to global buckling, a criterion now adopted in the latest draft of AISC Design Guide 38. Wang et al. [12] introduced a replaceable bolted built-up double-corrugated shear wall; experiments showed that increasing wave height from 40 to 60 mm raises ultimate drift capacity by 18% and keeps residual strength above 0.8 Vmax after three replacement cycles, providing a resilient solution for high-seismic regions. For conventional frame structures, optimization studies have centered on reliability and collapse safety: researchers have developed metamodel and metaheuristic-based methods for reliability-oriented optimum seismic design of RC frames [13], while others have realized seismic collapse safety optimization for steel moment-resisting frames [14]. Yet these optimization approaches have not been extended to corrugated steel frame systems.

At present, systematic research on the dynamic characteristics of corrugated steel frame structures remains limited, particularly regarding the optimization of geometric parameters and seismic performance under different ground motion records. To address these gaps, this study conducted a systematic numerical and parametric investigation into the dynamic behavior of steel frames with trapezoidal corrugated webs. Methodologically, a three-story numerical model was established in ABAQUS, and modal analysis, elasto-plastic time-history analysis under two typical seismic waves [15–17], and the control variable method were employed to examine the relationships between geometric parameters and structural performance, as shown in Fig. 1 (Analysis Method Flow Chart). This research elucidated the influence of key parameters—web thickness, corrugation angle, wavelength, and wave height—on seismic response, and compared structural behavior under the two typical seismic records. The results identified an optimized parameter combination that improves dynamic performance, highlighted the critical importance of the Ux direction in seismic design, and thus provided a theoretical basis for advancing the engineering application of corrugated steel structures. The core innovation is shifting from component-level to system-level analysis and comprehensively assessing the seismic characteristics of corrugated steel frame structures under two typical seismic waves, thereby addressing the current lack of research on the dynamic performance of such structural systems.

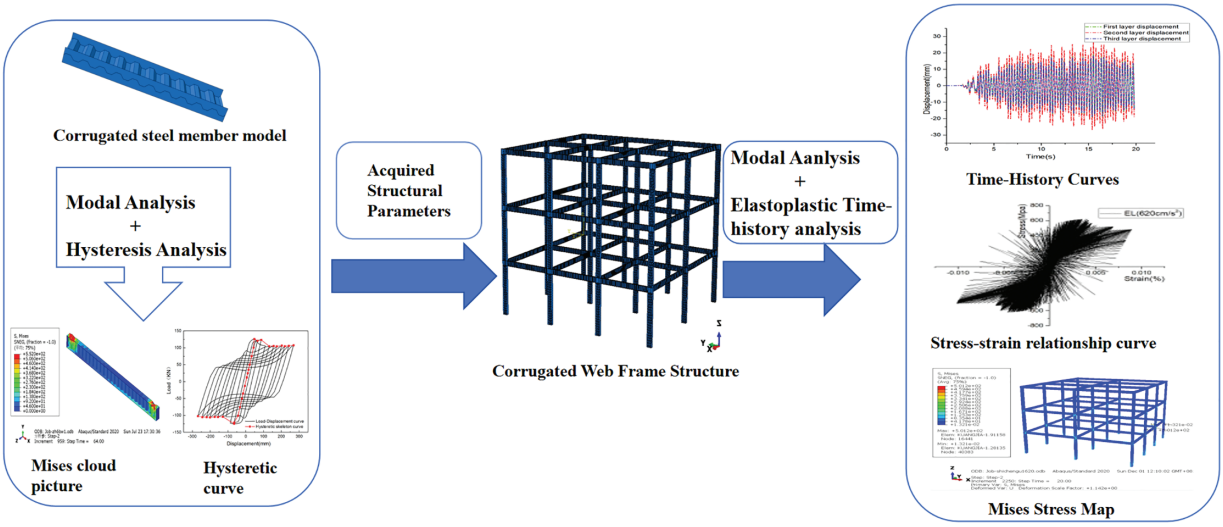

Figure 1: Analysis method flow chart

2 Material Constitutive Relation and Model

The research model was developed using the ABAQUS finite element software [18,19]. S4R shell elements were adopted, and the steel constitutive model is illustrated in Fig. 2 [20–22]. Material parameters are listed in Table 1, while Table 2 presents the corrugation parameters of the web employed in this study; Fig. 3 is a schematic diagram of the corrugation form of the steel member, and Fig. 4 shows the simulation model of the member. To ensure analytical reliability, a mesh sensitivity analysis was performed on the simulation model to mitigate mesh-dependent errors, with targeted refinement applied to the corrugation folds. After testing multiple mesh densities, the results were deemed converged if the maximum relative difference in stress at the corrugation folds between two consecutive refined schemes was $\leq 3\%$.

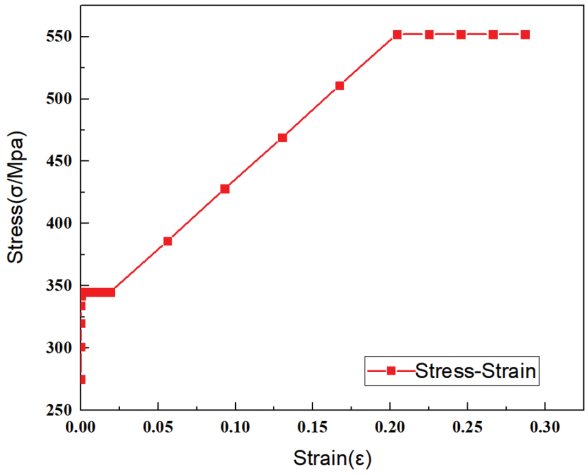

Figure 2: Material ontological model [23]

Table 1: Material parameters

Seels	Modulus of elasticity	Density	Poisson's ratio	Design value of tensile strength
Q345	2.06×10^{11} N/m^2	7850 kg/m^3	0.28	310 N/mm^2

Table 2: Reference table of geometric parameters for corrugated steel

(a × b) (mm × mm)	(h × c) (mm × mm)	θ (°)	d/2 (mm)	λ (mm × mm)	L (mm)	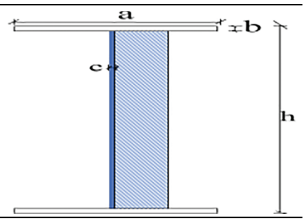
200 × 10	520 × 2	45	25	240	1290	corrugated steel section

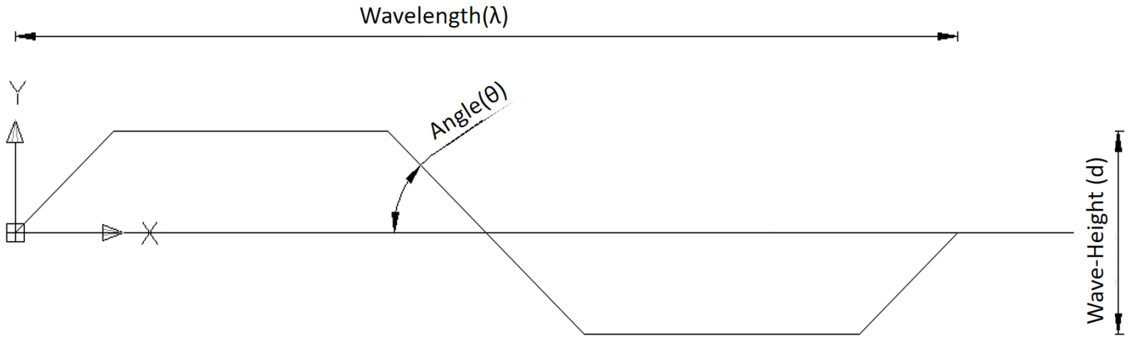

Figure 3: Diagram of the waveform of the abdominal plate

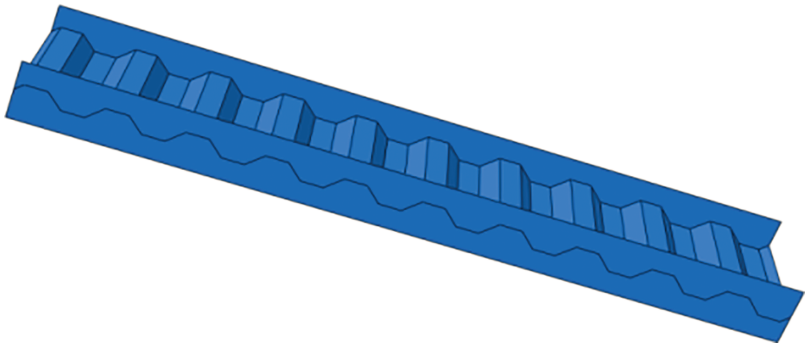

Figure 4: Trapezoidal corrugated steel member model

3 Influence Analysis of Corrugated Steel Structural Parameters on Modal Characteristics

With reference to the original parameters in Table 2, the control variable method was employed to alter each parameter sequentially to observe the variation patterns in the modal characteristics of the trapezoidal corrugated web H-shaped steel members. The web's corrugation profile is illustrated in Fig. 2.

3.1 The Influence of Web Thickness

The variation pattern of the component's modal characteristics was investigated by varying the web thickness. The thickness (c) values employed were 2, 2.5, 3, 3.5, 4, 4.5, 5, 5.5, and 6 mm.

As shown in Fig. 5, with other design parameters kept constant, an increase in web thickness results in a marginal reduction in the first two natural frequencies of the component, while inducing a more pronounced increase in the subsequent four modes. Although a slight reduction is observed in the lower-order frequencies, the marked upward shift in the higher-order modes suggests that web thickening generally elevates the natural frequencies of the component.

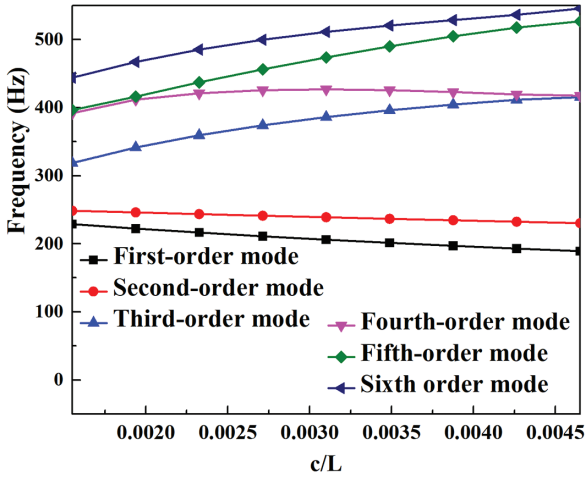

Figure 5: Variation of frequency with web thickness of the component

The rise in natural frequencies contributes to avoiding resonance with external excitation sources, thereby reducing the risk of vibration-induced fatigue, damage, and related instability. Together with the improved structural stiffness and load-bearing capacity provided by thicker webs, this evidence supports the conclusion that increasing web thickness represents an effective and practicable strategy for enhancing structural stability during the design phase.

3.2 The Influence of Corrugation Angle

The variation in the component's modal characteristics was investigated for corrugation angles (θ) of 22.5°, 30°, 45°, 60°, 75°, and 90°. This parameter range captures the full transition of the web profile from triangular to trapezoidal and finally to rectangular.

As shown in Fig. 6, the natural frequencies of the first three modes remain largely insensitive to variations in the corrugation angle. In contrast, the frequencies of the higher-order modes exhibit an initial increase followed by stabilization as the angle increases.

Given that the dynamic characteristics here are predominantly influenced by higher-order mode behavior, the optimal corrugation angle should be selected based on their frequency responses. It is noted that when the θ/L ratio ranges from 0.035 (45°) to 0.058 (75°), the natural frequencies of the fourth-, fifth-, and sixth-order modes remain stably elevated. This reduces resonance risk, enhances vibration resistance, and denotes favorable dynamic performance. Thus, a corrugation angle of 45°–75° is recommended to achieve the component's optimal dynamic characteristics.

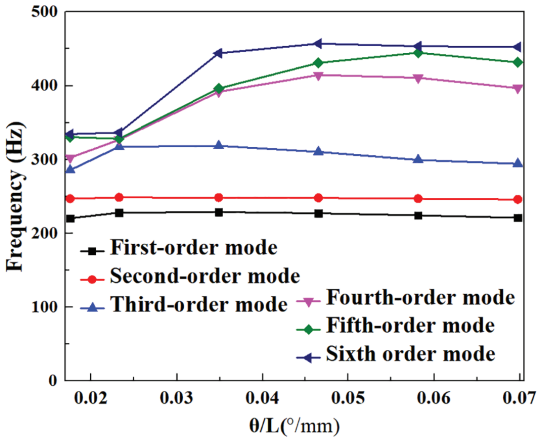

Figure 6: Variation of frequency with the component's corrugation angle

3.3 The Influence of Corrugation Wavelength

The variation in the component's performance was investigated across a range of corrugated web wavelengths, specifically $\lambda = 150$, 180, 210, 240, 270, and 300 mm. The results are illustrated in Fig. 7.

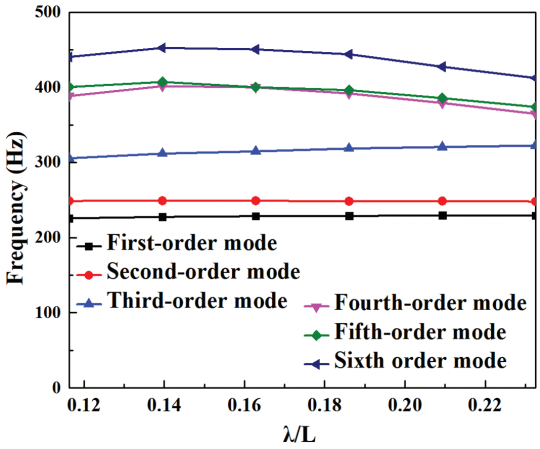

Figure 7: Variation of frequency with the component's web wavelength

As shown in Fig. 7, the natural frequency for all modal orders of the corrugated web H-shaped steel member exhibits a decreasing trend with increasing web wavelength. Therefore, to enhance both the natural frequency and structural stability of the member, it is recommended to reduce the web wavelength.

3.4 The Influence of Corrugation Height

The behavior of the component is presented as a function of the web corrugation height, where the d/2 values are 10, 20, 30, 40, 50, and 60 mm.

Fig. 8 shows that the natural frequency initially increases, peaks at a corrugation height of 30 mm (d/2L = 0.023), and then decreases before stabilizing, indicating that the structural stiffness first increases and then decreases. Consequently, deformation is minimized at this optimal height of 30 mm, which also delivers the best stability.

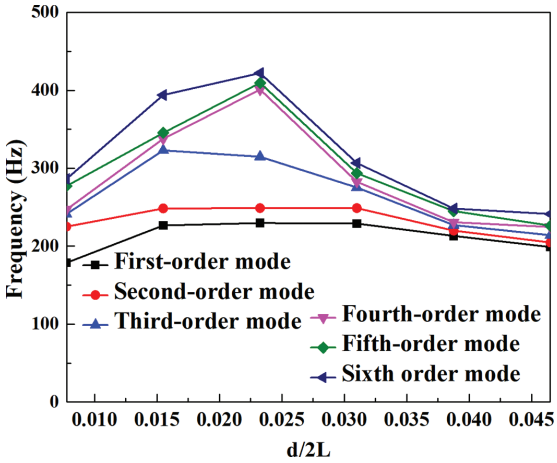

Figure 8: Variation of frequency with the component's corrugation height

The analysis, with other parameters held constant, yields the following conclusions:

Web thickness: Under certain conditions, increasing the web thickness enhances structural stability.

Corrugation angle: 45°–75° (favorable dynamic performance of the component).

Corrugation wavelength: To improve the natural frequency and stability of the structure, the wavelength should not be too long.

Corrugated height: Optimal stiffness and stability of the structural component are achieved at $d/2 = 30$ mm.

4 Quasi-Static Analysis of Corrugated Steel Members

To further investigate the ductility and energy dissipation capacity of corrugated steel, a low-cycle fatigue test was conducted on a corrugated steel frame using a simplified model—with key loading protocol detailed as follows: one end of the model was fully fixed (constraining all six degrees of freedom) while cyclic load was applied to the free end; under a constant axial compression ratio, displacement-controlled loading (perpendicular to the beam axis) was adopted, and as shown in Fig. 9, the displacement started from 0 mm and was incrementally increased to 180 mm, with one complete loading-unloading cycle implemented every 4 s, and the time duration corresponding to each displacement amplitude predefined in the analysis steps [24,25].

From the hysteretic curves and von Mises stress nephograms shown in Figs. 10 and 11, it can be observed that: the hysteretic curves are plump with only a slight pinching phenomenon. This slight pinching is mainly attributed to local stress concentration and minor slip at the beam ends (the initial failure regions) under cyclic loading, coupled with the constraint imposed by the constant axial compression ratio on the member's lateral deformation. Nevertheless, the plump hysteretic curves indicate that corrugated steel members possess excellent ductility and energy dissipation capacity—a direct manifestation of their key seismic performance. Their skeleton curves fully exhibit three typical developmental stages: elastic, elastoplastic, and plastic [26]. In terms of failure characteristics, the local areas at both ends of the beam are the first to reach the yield limit and initiate failure. This phenomenon is consistent with the mechanical property evolution of conventional steel structural members, which lays a foundation for subsequent analyses.

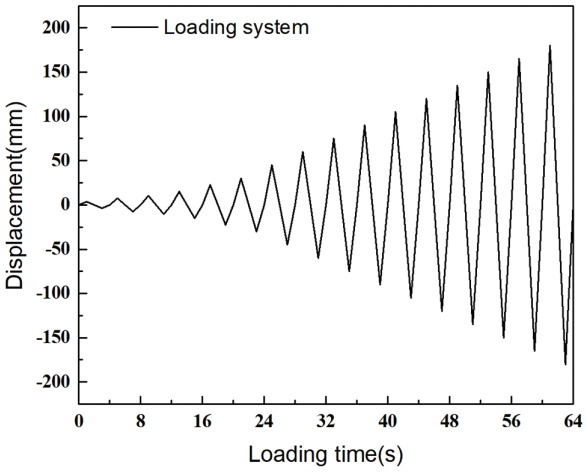

Figure 9: Loading system

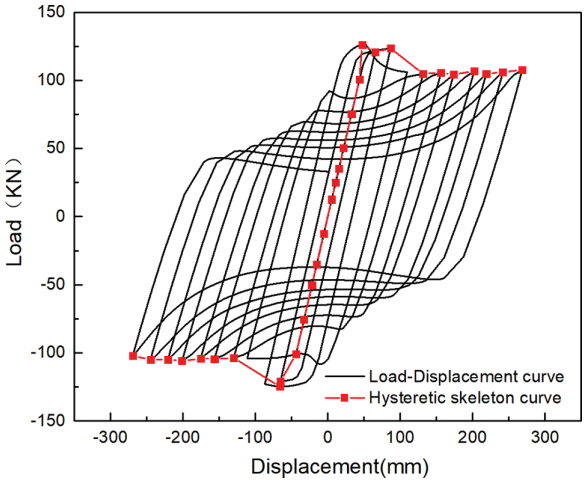

Figure 10: Hysteretic curve

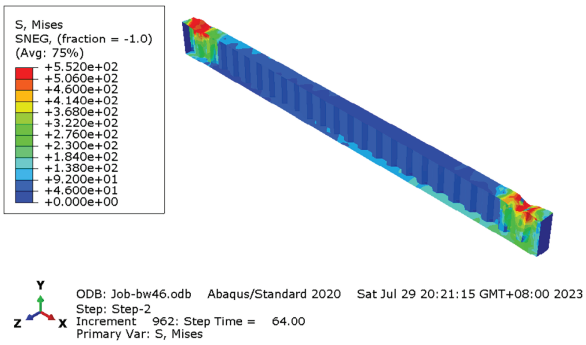

Figure 11: Mises cloud picture

5 Dynamic Performance and Failure Mechanism of Corrugated Steel Web Frame Structures

Based on the preceding calculations, corrugated steel members with a web thickness of 2 mm, a corrugation angle of 45°, a wavelength of 240 mm, and a corrugation height of 30 mm were adopted for fabricating the corrugated web frame structure. Specifically, the longitudinal beams span 9 m along the *y*-direction, the transverse beams span 6.5 m along the *x*-direction, and the columns have a height of 5 m. These dimensions fall within the reasonable span range (6–12 m) for conventional frames, satisfying both structural rationality and relevant code requirements.

The joints of the corrugated web frame structure employ flat web connections. The column bases are designed as fixed supports, where all degrees of freedom (Ux, Uy, Uz, UR1, UR2, UR3) are fully constrained. Numerical simulations were performed using the large-scale finite element software ABAQUS. The schematic diagram of the corrugated web H-section and the three-dimensional simulation model of the three-story frame are presented in Figs. 12 and 13 [27], respectively.

In this section, seismic waves are applied independently along the Ux and Uy directions to investigate the dynamic performance of the corrugated steel frame structure.

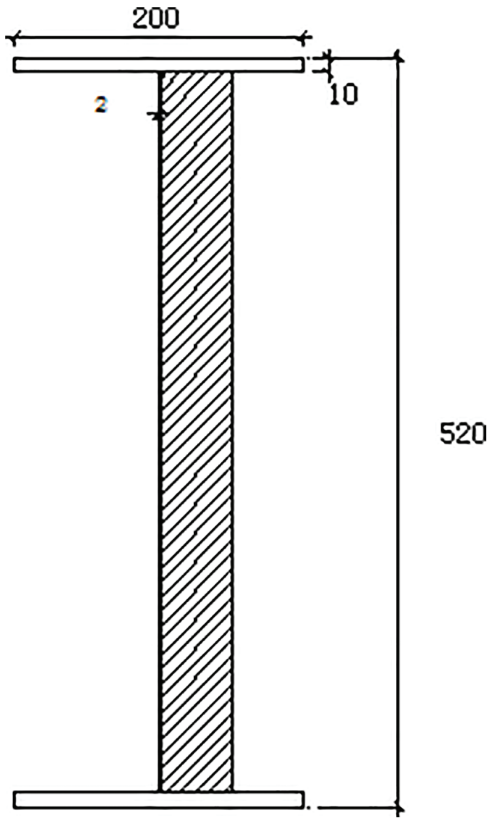

Figure 12: Corrugated web H-beam section

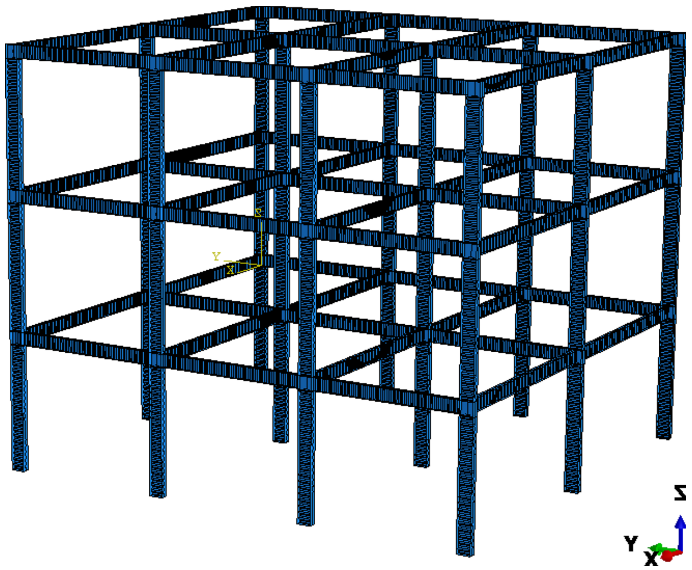

Figure 13: Simulation model of an H-shaped three-story frame structure with a corrugated belly plate

5.1 Modal Analysis of Frame Structure

The results of the modal analysis indicate that the first-order natural frequency of the frame model is 1.8686 Hz, corresponding to a period of 0.535 s. The error between this result and the calculation result of 0.526 s from the auxiliary software PKPM is within 5%, which verifies the reliability of the finite element model [28]. Table 3 presents the diagrams of the first four modal shapes and their corresponding natural frequencies. Specifically, the first-order modal shape exhibits overall translational characteristics, the second- and third-order modal shapes show torsional modes, and the higher-order modal shapes gradually present vertical vibration modes. The evolution regularity of each modal shape is consistent with the dynamic characteristics of conventional frame structures, and this sequence of modal development conforms to the typical dynamic response characteristics of multi-story frame structures, further confirming the rationality of the model development.

5.2 Dynamic Response under Earthquake Load

The El Centro wave and the Taft wave are typical ground motion records widely used in earthquake engineering. The El Centro wave is from the 1940 Imperial Valley earthquake (Mw 6.9, USA) with a peak ground acceleration (PGA) of 0.35 g, representing near-fault pulse-type ground motion with distinct impulsive effects and rich high-frequency components [29]. The Taft wave is derived from the 1952 Kern County earthquake (Ms 7.4, USA), recorded 43.5 km from the epicenter with a PGA of 1.79 g, and it characterizes far-field earthquakes with prominent long-period components [30].

These two waves are specifically selected for three key reasons: first, they respectively cover the two most critical seismic scenarios in engineering—near-fault and far-field earthquakes; second, their spectral characteristics (high-frequency for El Centro vs. long-period for Taft) and dynamic parameters differ significantly, enabling comprehensive evaluation of the structure's adaptability to diverse excitations; third, as internationally recognized standard records, they ensure the comparability and credibility of the study results.

By analyzing the dynamic response of structures to these two seismic waves, the seismic performance of structures under earthquakes with different spectral characteristics can be evaluated [31–33].

In this study, the El Centro and Taft seismic waves will be applied along the Ux and Uy directions of the frame structure, respectively. The elastoplastic time-history analysis method will then be used to examine the dynamic performance of the structure under both waves.

Table 3: Mode shape and natural frequency

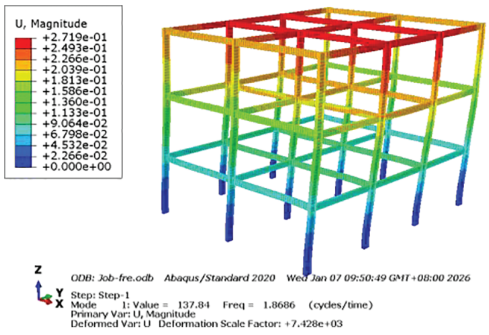

First-order mode shape; Freq = 1.8686

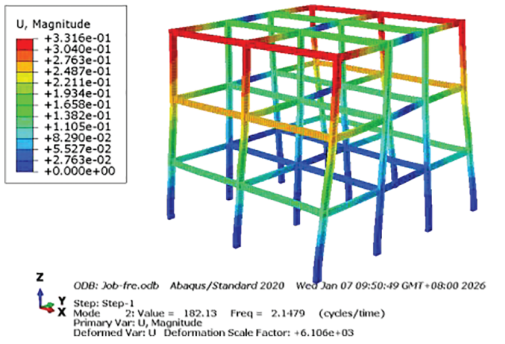

Second-order mode shape; Freq = 2.1479

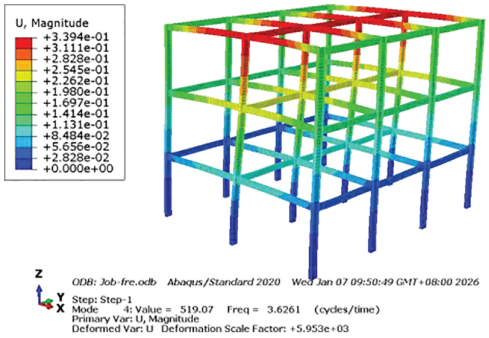

Third-order mode shape; Freq = 2.8315

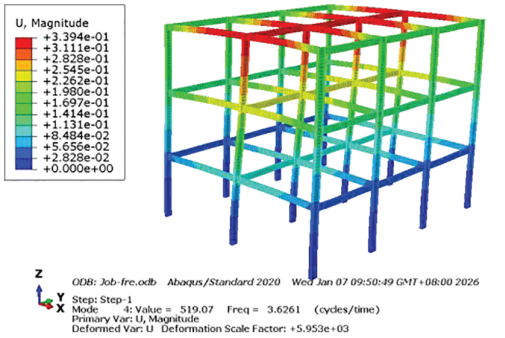

Fourth-order mode shape; Freq = 3.6261

5.2.1 Dynamic Performance of a Frame Structure under Seismic Excitation in the Ux Direction

The following presents the results from applying seismic waves in the Ux direction. Tables 4 and 5 present the time-history curves and inter-story drift comparisons, respectively, for the structure under seismic excitations of different intensities. The analysis of the structural response reveals the following for the three-story corrugated steel frame under Ux-directional seismic waves: Under both El Centro (near-fault pulse-type) and Taft (far-field long-period) ground motions, the inter-story drift at each story increases monotonically with the Peak Ground Acceleration (PGA). At the same PGA level, the drift induced by El Centro is significantly larger than that induced by Taft, and it exhibits a faster growth rate as PGA increases—underscoring the strong amplification effect of near-fault pulses on structural deformation.

As specified in the *Code for Seismic Design of Buildings (GB50011)*, the elastoplastic inter-story drift limit for this structure is 100 mm. Under the PGA level corresponding to an 8-degree rare earthquake, the drift under El Centro excitation exceeds this limit, indicating that the structure fails to meet the seismic design requirements for near-fault scenarios. In contrast, under Taft excitation, the drift at each story remains within the limit, thus satisfying the requirements for far-field earthquake scenarios.

Table 4: Time-history curves for each story under El centro and taft waves

PGA (cm/s^2)	220	310	400	510	620
el-centro	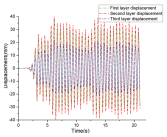	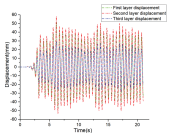	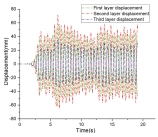	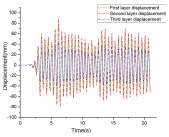	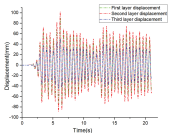
Taft	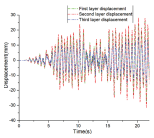	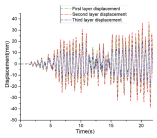	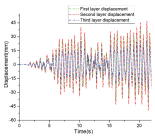	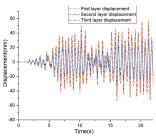	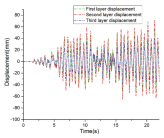

Table 5: Comparison of inter-story displacements for the El centro and taft waves

PGA	EL Centro (Ux)			Taft (Ux)		
(cm/s^2)	*Ux* (mm)			*Ux* (mm)		
	1st story	2nd story	3rd story	1st story	2nd story	3rd story
220	37.26	42.6	21.68	25.73	29.38	14.98
310	51.17	57.62	29.14	35.31	41.22	21.23
400	63.24	72.31	31.47	46.26	51.92	27.52
510	77.37	89.35	46.71	51.42	60.64	32.57
620	89.72	101.89	50.82	58.96	71.46	39.91

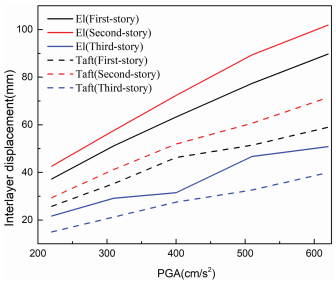

This difference arises because the high-frequency pulse components in El Centro readily induce significant plastic deformation in the structure, whereas the long-period components in Taft affect the three-story frame only mildly. Subsequent design should, therefore, focus on strengthening the structure against near-fault pulse-type ground motions. Measures may include increasing member cross-sections, optimizing corrugated web parameters to improve lateral stiffness, or enhancing joint ductility to increase energy dissipation capacity. These improvements will ensure the structure meets the code-specified seismic performance objectives under various earthquake scenarios.

As shown in Table 6, the three-story corrugated steel frame structure exhibits distinctly different nonlinear response patterns under El Centro near-fault pulse-type ground motion and Taft far-field long-period ground motion. The high-frequency pulse characteristics of the El Centro wave induce stress-strain cycles with larger amplitudes, resulting in fuller hysteretic loops and strong energy dissipation capacity, but simultaneously lead to more significant cumulative plastic damage. In contrast, the long-period components of the Taft wave only trigger small-magnitude stress-strain fluctuations, forming compact hysteretic loops with lower energy dissipation efficiency and relatively controllable plastic damage.

Table 6: Stress-strain relationship at peak stress under different seismic waves

PGA (cm/s^2)	220	310	400	510	620
el-centro	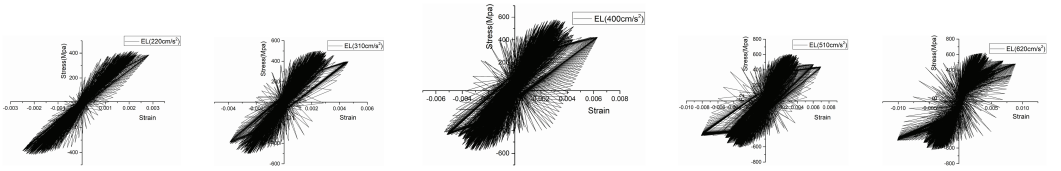				
Taft	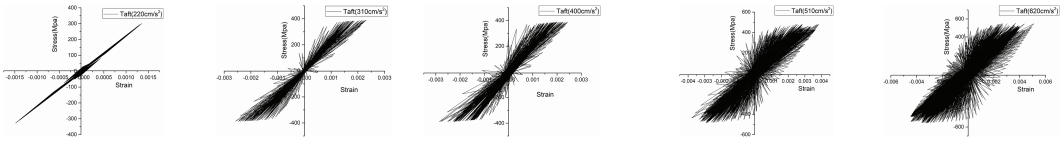				

Tables 7 and 8 further indicate that the variation law of peak stress with peak ground acceleration (PGA) also presents obvious differences: under the El Centro wave, the peak stress increases nonlinearly and features a "plateau phase" (characterizing structural yielding or softening) within the PGA range of 310–400 cm/s^2, after which the growth rate slows significantly. Under the Taft wave, the peak stress exhibits a three-stage characteristic—"rapid rise–stable growth–reacceleration under high PGA levels"—reflecting that its low-frequency components effectively excite the structure's higher-order modes under high-intensity excitation, thereby enhancing structural response.

Table 7: Comparison of stress cloud maps

PGA (cm/s^2)	el-centro	Taft
220	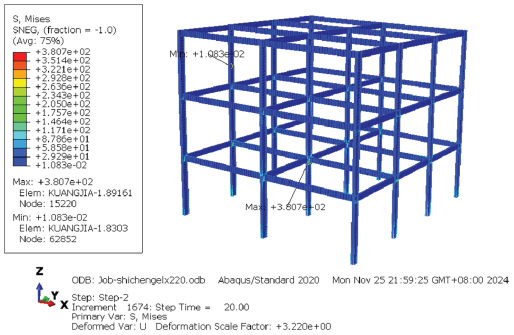	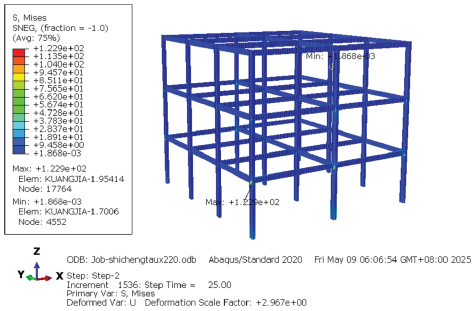
620	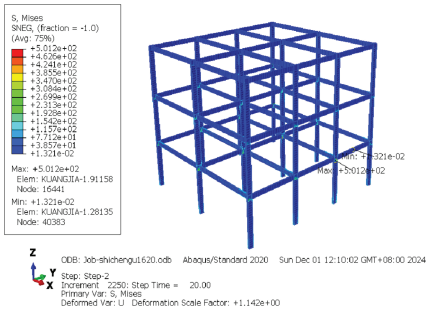	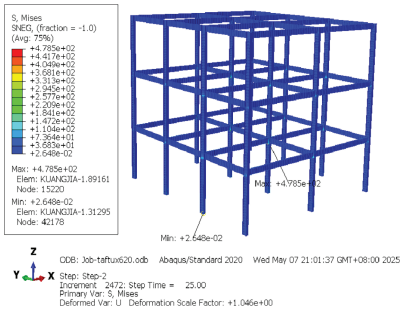

Table 8: Peak stresses under different seismic waves (MPa)

PGA (cm/s²)	220	310	400	510	620
EL-centro (Ux)	380.7	433.0	437.6	472.4	501.2
Taft (Ux)	122.9	291.2	349.1	380.8	478.5

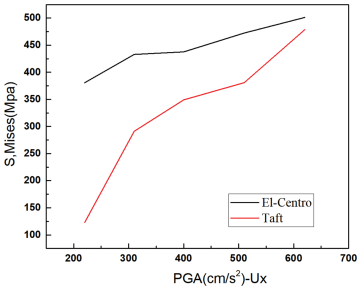

These differences illustrate that the high-frequency components of the El Centro wave easily resonate with the structure's lower-order modes, inducing plastic deformation at an early stage. The low-frequency components of the Taft wave have weak coupling with the structure under low PGA (evidenced by small stress-strain variation amplitudes and compact hysteretic loops) but can significantly activate higher-order modes under high PGA. Based on this, it is recommended that in the design of near-fault regions, a balance between energy dissipation capacity and damage control should be achieved through optimizing corrugated web parameters and joint ductility. In regions dominated by far-field long-period earthquakes, constraints on higher-order modes and lateral stiffness under high PGA should be strengthened to ensure the stable seismic performance of the structure under ground motions with different spectral characteristics.

5.2.2 Dynamic Performance of a Frame Structure under Seismic Excitation in the Uy Direction

The following presents the results from applying seismic waves in the Uy direction. As shown in Tables 9 and 10, under Uy-directional seismic ground motion, the inter-story displacements of each floor in the three-story corrugated steel frame monotonically increase with peak ground acceleration (PGA, 220–620 cm/s²), exhibiting a phased characteristic of "rapid growth at low PGA, slowed growth at medium PGA, and stable growth at high PGA." This reflects the structure's transition from an elastic to a weakly plastic working state. At the same PGA level, the displacements induced by Taft far-field long-period ground motion are generally larger than those by El Centro near-fault pulse-type ground motion, with the root cause lying in the fact that the low-frequency components of the Taft wave are more likely to couple and resonate with the natural frequency of the structure in the Uy direction. Additionally, under both ground motions, the inter-story displacements of the structure are less than 100 mm, meeting the requirements of the Seismic Design Code.

Under all loading conditions, the Uy-directional displacement of the 2nd floor is consistently the maximum among all floors, with the displacement ratio to the 1st and 3rd floors stably ranging from 1.40 to 1.53. Combined with the structural mechanical constraint characteristics and modal response mechanism, it can be determined that the 2nd floor is the absolute weak story in the Uy direction—this conclusion is consistent with the weak story identification criteria specified in the code.

For this frame structure, the seismic design should prioritize improving the out-of-plane stiffness and joint ductility of the beams and columns on the 2nd floor, controlling the cumulative damage of the weak story, thereby ensuring the overall stability of the structure under complex seismic scenarios.

Table 9: Time-history curves for each story under El centro and taft waves

PGA (cm/s^2)	220	310	400	510	620
el-centro	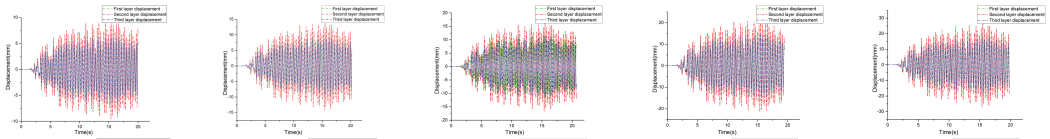				
Taft	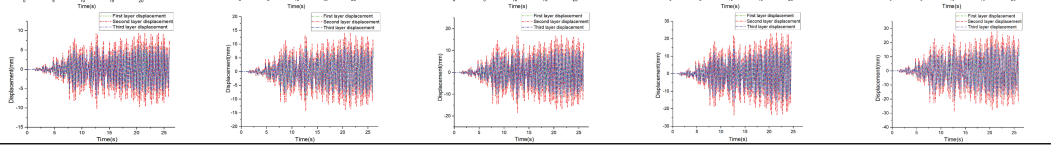				

Table 10: Comparison of inter-story displacements for the El-centro and taft waves

PGA	EL-centro (Uy)			Taft (Uy)		
(cm/s^2)	Uy (mm)			Uy (mm)		
	1st story	2nd story	3rd story	1st story	2nd story	3rd story
220	6.79	9.58	6.69	7.54	10.28	6.92
310	10.05	14.32	9.46	10.55	14.42	9.69
400	11.95	16.67	11.51	13.51	18.45	12.36
510	15.26	21.35	15.17	17.16	23.71	16.3
620	19.35	27.11	18.72	21.0	28.9	19.9

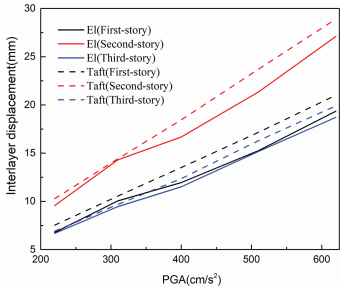

Tables 11–13 reveal distinct structural response characteristics of the structure under El Centro near-fault pulse-type and Taft far-field long-period ground motions. Specifically, as shown in Table 12, under El Centro ground motion, the stress-strain hysteretic loops gradually expand and develop multi-branched features with increasing peak ground acceleration (PGA). This phenomenon indicates significant seismic energy dissipation capacity, while also reflecting pronounced cumulative plastic damage—particularly after the structure exhibits full elastoplastic behavior at a PGA of 620 cm/s^2. By contrast, Taft ground motion induces relatively gentle and concentrated hysteretic loops, which are indicative of limited energy dissipation efficiency.

As can be seen from Tables 11 and 13, the El Centro ground motion (near-fault pulse-type) causes significant fluctuations in the structure's Uy-direction displacement. At a peak ground acceleration (PGA) of approximately 400 cm/s^2, the displacement first decreases by 41% and then surges by 271%, a result of the mutual cancellation and superposition of vibrations in different parts of the structure. This PGA value of 400 cm/s^2 is the multi-mode coupling threshold, marking the structure's transition from vibration of only a few parts to vibration of multiple interacting parts. In contrast, the Taft ground motion (far-field long-period-type) exhibits a more conventional displacement trend of "increase followed by decrease." The displacement peaks at a PGA of 510 cm/s^2, which is the yield point where

the structure begins to undergo plastic deformation. After that, the displacement decreases because the structure's natural vibration frequency shifts away from the dominant energy band of the Taft ground motion following plastic deformation, leading to reduced vibration.

Table 11: Comparison of stress cloud maps

PGA (cm/s^2)	el-centro	Taft
220	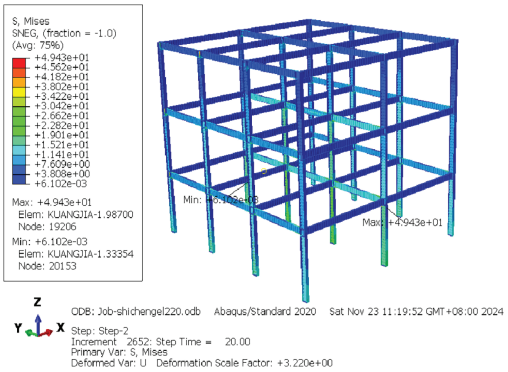	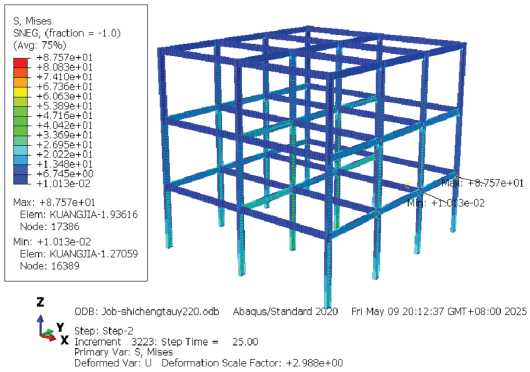
620	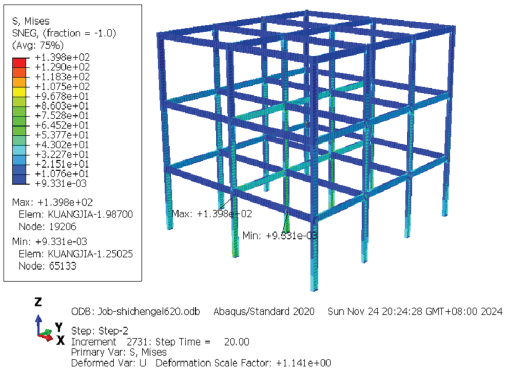	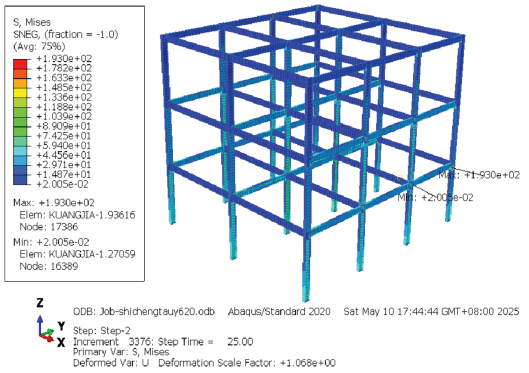

Table 12: Stress-strain relationship at peak stress under different seismic waves

PGA (cm/s^2)	220	310	400	510	620
el-centro	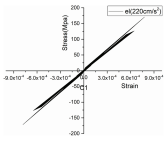	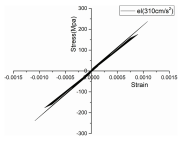	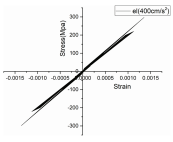	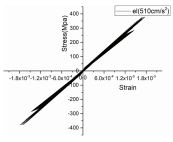	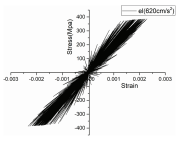
Taft	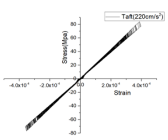	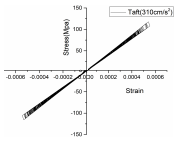	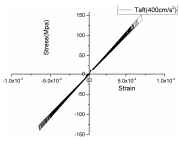	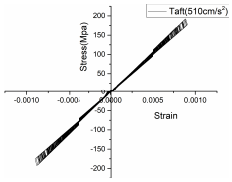	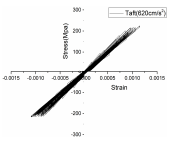

Table 13: Peak stresses under different seismic waves (MPa)

PGA (cm/s²)	220	310	400	510	620
EL Centro (UY)	49.43	29.24	108.5	89.96	139.8
Taft (UY)	87.57	89.2	147.0	228.9	193.0

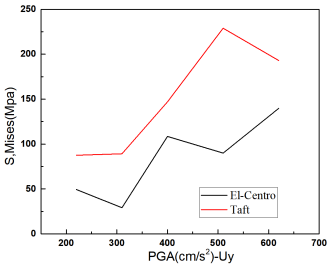

These results confirm that the broad-frequency El Centro ground motion excites complex multi-modal responses in the structure, whereas the narrow-band Taft ground motion induces relatively simple single-mode-dominated behavior. The spectral compatibility between ground motion and structural dynamic characteristics thus emerges as the core factor governing the structural seismic response patterns.

5.2.3 Dynamic Performance of Frame Structure in Ux and Uy Directions

This section analyzes the dynamic response of the structure under simultaneous Ux- and Uy-directional seismic excitation. As indicated by the comparison of structural stresses in each direction under bidirectional (Ux–Uy) seismic excitation (Table 14), the mechanical response in the Ux direction is significantly more pronounced. This phenomenon is primarily attributed to the coupled effects of three key factors: first, the structure exhibits lower lateral stiffness in the Ux direction (a result of sparser component layouts, e.g., larger column spacing), rendering it more susceptible to resonance with the energy-dominant frequency band of seismic waves; second, the Ux direction undergoes more significant seismic energy input, particularly for near-fault waves; and third, more extensive plastic development in the Ux direction further amplifies the response. Therefore, in accordance with the principle of prioritizing the analysis of the most critical structural conditions, the Ux direction is selected as the primary direction for graphical presentation.

Based on Tables 15 and 16, the Ux displacement responses of Floors 1–3 under two seismic waves are summarized below: Under the El Centro wave, Ux displacements increase monotonically with PGA (220–620 cm/s²), following the order: Story 2 > Story 1 > Story 3. The growth rates are 136.7%, 145.9%, and 148.2% for Floors 1, 2, and 3, respectively, with Floor 3 showing the highest sensitivity. Bidirectional excitation produces slightly larger displacements than unidirectional cases.

Under the Taft wave, Ux displacements also increase monotonically with PGA, maintaining the same floor order. Growth rates reach 169.4%, 144.8%, and 159.1% for Floors 1, 2, and 3, respectively, with Floor 1 exhibiting the most significant response. Displacements are generally smaller than under the El Centro wave, except for Floor 2 at 620 cm/s². The sustained growth indicates elastic structural behavior. As with El Centro, bidirectional loading causes larger displacements. According to the provisions of the *Code for Seismic Design of Buildings*, at the PGA corresponding to an 8-degree rare earthquake, the displacement of 103.74 mm under El Centro excitation exceeds the specified limit value of 100 mm. This indicates that the structure fails to meet the seismic design requirements for near-fault scenarios. In contrast, under Taft excitation, the inter-story drift of each floor falls within the limit range, thus satisfying the requirements for far-field seismic scenarios. This conclusion is consistent with that of the unidirectional excitation in the Ux direction.

Table 14: Comparison of maximum stresses under bidirectional seismic loading (Ux and Uy Directions)

PGA (cm/s^2)	220	310	400	510	620
EL-centro (Ux)	246.1	330.2	405.5	433.9	500.7
Taft (Ux)	249.9	364.4	391.1	463.6	526.5
EL-centro (Uy)	192.8	257.5	302.5	347.3	319.7
Taft (Uy)	152.8	193.9	273.3	329.9	383.2
EL-centro (U)	244.1	326.2	398.7	431.4	475.9
Taft (U)	231.6	338.3	365.0	428.0	496.0

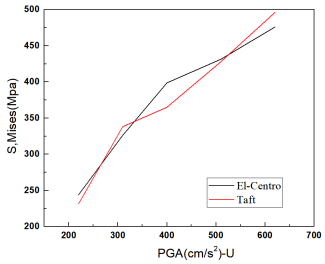

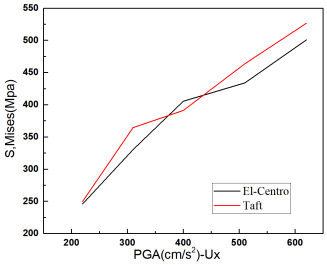

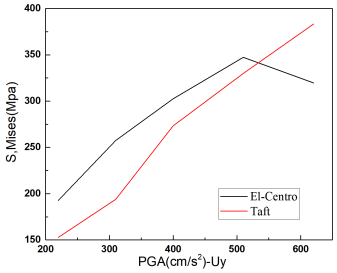

Table 15: Time-history curves for each story under El centro and taft waves (Ux Directions)

PGA (cm/s^2)	220	310	400	510	620
el-centro	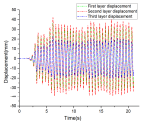	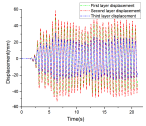	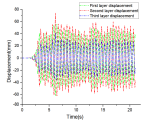	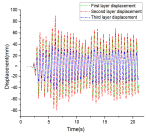	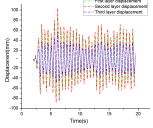
Taft	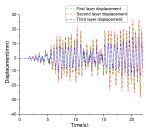	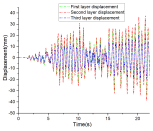	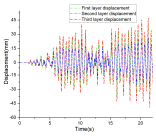	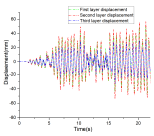	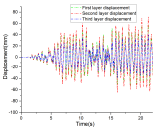

Table 16: Inter-story displacements in the Ux direction for different seismic waves (Ux Directions)

PGA	EL-centro			Taft		
(cm/s²)	*Ux* (mm)			*Ux* (mm)		
	1st story	2nd story	3rd story	1st story	2nd story	3rd story
220	36.63	42.19	22.86	22.43	26.91	15.61
310	50.33	58.49	31.65	31.97	37.78	21.27
400	61.67	73.82	41.04	39.39	47.3	27.52
510	76.27	89.96	49.54	49.8	55.59	33.27
620	86.71	103.74	56.74	60.43	65.88	40.45

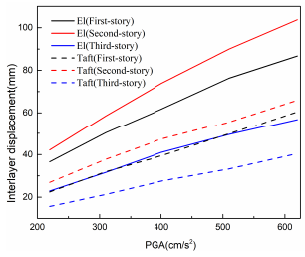

Comparative analysis shows that El Centro produces larger displacements on Floors 1 and 3, while for Floor 2, displacements converge at high PGA. The El Centro wave more strongly affects lower floors, whereas the Taft wave causes higher sensitivity on Floor 1. These results confirm that seismic spectral characteristics differentially influence floor-specific displacement responses.

As shown in Table 17, both nonlinear deformation and energy dissipation demand increase with PGA under both seismic waves, with growth being faster under the El Centro wave. At identical PGA levels, the hysteretic loops under El Centro excitation are fuller and more dispersed, indicating stronger nonlinear energy dissipation capacity. In contrast, those under the Taft wave appear narrower and more compact, suggesting predominantly elastic or weakly nonlinear structural behavior.

Table 17: Stress-strain relationship at peak stress under different seismic waves (Ux Directions)

PGA (cm/s²)	220	310	400	510	620
el-centro	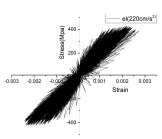	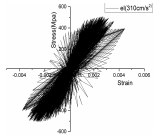	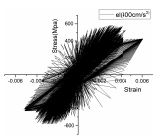	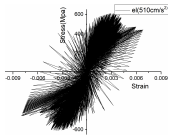	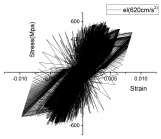
Taft	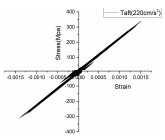	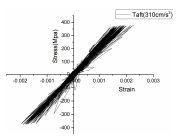	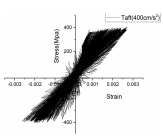	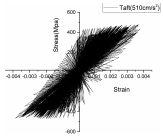	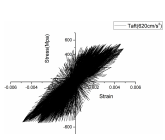

Note: The stress-strain curve is obtained at the peak stress (S11).

According to Tables 14 and 18, under the El Centro wave, the Ux-direction stress increases monotonically by 103.4% with increasing PGA. The Uy-direction stress rises by 80.2% as PGA increases from 220 to 510 cm/s², then decreases by 8.0% at 620 cm/s², which is attributed to broad-spectrum characteristics inducing multi-modal coupling (Multiple vibration modes interact with each

other)and stiffness degradation. The resultant stress is dominated by the Ux component and follows a similar trend.

Table 18: Comparison of stress cloud maps (Resultant displacement in U Directions)

PGA (cm/s^2)	el-centro	Taft
220	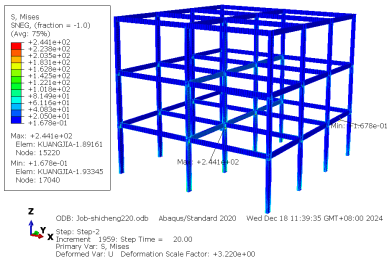	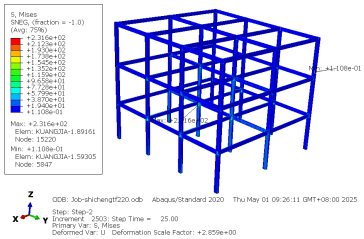
620	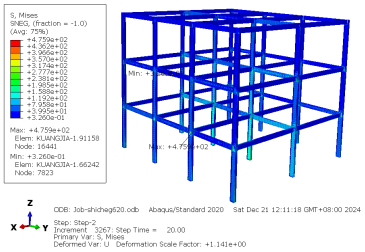	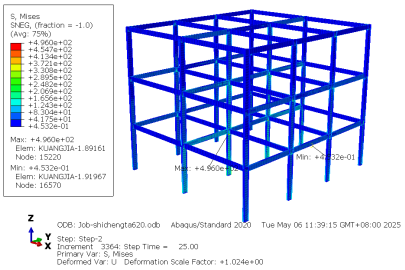

Under the Taft wave, stresses in the Ux, Uy, and U directions increase by 110.7%, 150.8%, and 114.2%, respectively. The notably higher growth in the Uy direction results from continuous excitation by the wave's concentrated energy band while the structure remains elastic.

Comparative analysis identifies a transition at PGA = 510 cm/s^2. Below this threshold, the El Centro wave produces lower stresses in the Ux and U directions, whereas the Taft wave results in lower Uy-direction stress. Beyond this point, the Taft wave induces comprehensively higher stresses in all directions, with a 20.0% difference observed in the Uy direction at 620 cm/s^2. These patterns confirm that the spectral characteristics of seismic waves—broad-spectrum vs. energy-concentrated—and their interaction with structural properties decisively influence the structural response patterns.

6 Conclusions

In this study, reasonable and feasible geometric parameter combinations were screened and finalized through geometric parameter analysis. Based on this, a three-story frame structure model that meets the numerical calculation accuracy requirements was established. We systematically investigated the dynamic response characteristics of this frame structure under excitation of the El Centro wave and the Taft wave, as well as the impact mechanism of seismic wave spectral characteristics on the overall dynamic behavior of the structure. The main research results are as follows:

(1) Using the control variable method, a study on H-shaped steel members with corrugated steel webs shows that when the thickness of the trapezoidal corrugated web is 2 mm, the member exhibits relatively good stability with a corrugation angle of 45°∼75°, a wave height of about 30 mm, and a wavelength of approximately 240 mm.

(2) Nonlinear time-history analyses performed in ABAQUS for the selected frame structure yield the following key findings:
   (a) The high-frequency pulses of the near-fault El Centro wave induce significant plastic damage in the structure, whereas the long-period components of the far-field Taft wave primarily elicit elastic responses—reflecting distinct stress evolution mechanisms. Quantitatively, under the El Centro wave with a peak ground acceleration (PGA) of 620 cm/s^2, the second-story drift reaches 101.89 mm, which exceeds the code-specified limit and thus fails to meet the seismic requirements for a rare intensity 8 earthquake.
   (b) Under seismic excitation along the Uy direction, the structure exhibits a transition from elastic to weakly plastic behavior, with the second story identified as the distinct vulnerable story. The low-frequency components of the Taft wave are prone to resonating with the natural frequency of the structure in the Uy direction, while the El Centro wave tends to trigger multimodal coupling. Overall, however, the structural response in the Uy direction remains relatively moderate, and inter-story drifts under all PGA levels are below 100 mm, satisfying the seismic code requirements.
   (c) Under bidirectional (Ux–Uy) seismic excitation, the structural response is dominated by the Ux direction, with inter-story drifts generally slightly larger than those under unidirectional (Ux or Uy) input. The broad-spectrum characteristics of the El Centro wave tend to induce multimodal coupling and stiffness degradation, whereas the narrow-band concentrated energy characteristics of the Taft wave lead to sustained structural oscillations. Quantitatively, under the El Centro wave with a peak ground acceleration (PGA) of 620 cm/s^2, the second-story drift reaches 103.74 mm, again failing to meet the seismic requirements for a rare intensity 8 earthquake.

In summary, the structural response is governed by the matching level between the seismic wave spectrum and the dynamic characteristics of the structure. In engineering design, for regions dominated by near-fault ground motions (e.g., El Centro-type), priority should be given to enhancing the stiffness and stability in the Ux (longitudinal) direction. For regions dominated by far-field ground motions (e.g., Taft-type), the Uy (transverse) stiffness should be strengthened under high PGA levels, and special attention should also be paid to the stiffness and ductility of the middle story.

Acknowledgement: Not applicable.

Funding Statement: This work was supported by the Scientific Research Program Funded by Education Department of Shaanxi Provincial Government (Program No. 25JK0544).

Author Contributions: The authors confirm contribution to the paper as follows: Writing, review, data curation, and editing, Huimin Cao; Review, funding acquisition, and data curation, Xiaoliang Yao; Software, Xuan Cui; Investigation and resources, Hui Lu; Software and validation, Yaping Xu; Funding acquisition, supervision, and figure, Xin-e Yan. All authors reviewed the results and approved the final version of the manuscript.

Availability of Data and Materials: The data that support the findings of this study are available from the Corresponding Author, [Huimin Cao], upon reasonable request.

Ethics Approval: Not applicable.

Conflicts of Interest: The authors declare no conflicts of interest to report regarding the present study.

References

1. Jelčić Rukavina M, Skejić D, Kralj A, Ščapec T, Milovanović B. Development of lightweight steel framed construction systems for nearly-zero energy buildings. Buildings. 2022;12(7):929. doi:10.3390/buildings12070929.
2. GB 50017-2017. Ministry of housing and urban-rural development of the People's Republic of China. Code for design of steel structures. Beijing, China: China Architecture & Building Press; 2017. (In Chinese).
3. Elgendy AH, El Hadidy AM, El-Boghdadi MH. Experimental study of lateral torsional buckling behaviour of mono-symmetric corrugated web girders. J Constr Steel Res. 2025;234:109694. doi:10.1016/j.jcsr.2025.109694.
4. Xie Y. Deep learning in earthquake engineering: a comprehensive review. arXiv:2405.09021. 2024. doi:10.48550/arxiv.2405.09021.
5. Mao YN, Ma C, Liu SZ, Li LY. Study on the dynamic response of composite box girder bridges with corrugated steel webs. Adv Civ Eng. 2023;2023:5104132. doi:10.1155/2023/5104132.
6. Cao K, Fu Q, Zhang J, Tang C, Huang J, Wang C, et al. Effect of corrugated steel angle on the damage characteristics and anti-explosion performance of corrugated steel-concrete composite structures. Struct Des Tall Build. 2024;33(11):e2112. doi:10.1002/tal.2112.
7. Li Y, Liu X, Zhai X, Yang T. Finite element analysis on the mechanical behaviors of new cross-slanted corrugated steel plate shear wall. IOP Conf Ser Earth Environ Sci. 2021;636(1):012030. doi:10.1088/1755-1315/636/1/012030.
8. Leblouba M, Barakat S, Altoubat S, Junaid TM, Maalej M. Normalized shear strength of trapezoidal corrugated steel webs. J Constr Steel Res. 2017;136:75–90. doi:10.1016/j.jcsr.2017.05.007.
9. Zhou M, An L. Full-range shear behavior of a nonprismatic beam with steel trapezoidal corrugated webs: experimental tests and FE modeling. J Struct Eng. 2020;146(8):04020162. doi:10.1061/(ASCE)ST.1943-541X.0002721.
10. Qiao H, Xu H, Zhang X, Xing Z, Chen Y, Tang E. Seismic performance of corrugated steel plate shear walls under various constraint conditions. Thin Walled Struct. 2023;192:111189. doi:10.1016/j.tws.2023.111189.
11. Leblouba M, Junaid MT, Barakat S, Altoubat S, Maalej M. Shear buckling and stress distribution in trapezoidal web corrugated steel beams. Thin Walled Struct. 2017;113:13–26. doi:10.1016/j.tws.2017.01.002.
12. Wang T, Zha Z, Bai Y, Guo T, Gao J, Ma J. Seismic performance of a novel replaceable bolted built-up double corrugated steel plate shear wall. Thin Walled Struct. 2025;217:113871. doi:10.1016/j.tws.2025.113871.
13. Gholizadeh S, Aligholizadeh V. Reliability-based optimum seismic design of RC frames by a metamodel and metaheuristics. Struct Des Tall Spec Build. 2019;28(1):e1552. doi:10.1002/tal.1552.
14. Gholizadeh S, Hasançebi O, Eser H, Koçkaya O. Seismic collapse safety based optimization of steel Moment-Resisting frames. Structures. 2022;45:329–42. doi:10.1016/j.istruc.2022.09.034.
15. Wang C, Ding X, Chen Z, Feng L, Han L. Seismic response of utility tunnels subjected to different earthquake excitations. Geomech Eng. 2021;24(1):67–79. doi:10.12989/GAE.2021.24.1.067.
16. Zhou X, Cheng X, Qi L, Wang P, Chai S, Liu Y. Shaking table model test of loess tunnel structure under rainfall. KSCE J Civ Eng. 2021;25(6):2225–38. doi:10.1007/s12205-021-1064-z.
17. Zou Z, Lei D, Jiang G, Luo B, Chang S, Hou C, et al. Experimental study of bridge foundation reinforced with front and back rows of anti-slide piles on gravel soil slope under el centro waves. Appl Sci. 2020;10(9):3108. doi:10.3390/app10093108.
18. Zhao H, Li YX, Wang YQ, Dong C, Guo Z, Zhang W. Study on crack extension in fatigue hazardous locations of crane truss based on ABAQUS-FRANC3D joint simulation. Ind Build. 2024:1–15. [cited 2025 Jan 1]. Available from: https://link.cnki.net/urlid/11.2068.TU.20240612.1151.004. (In Chinese).

19. Xiong X, Zheng Z. Finite element analysis of seismic behavior of PVA-ECC pier columns based on ABAQUS. Adv Eng Technol Res. 2023;7(1):334. doi:10.56028/aetr.7.1.334.2023.
20. Hartloper AR, de Castro e Sousa A, Lignos DG. Constitutive modeling of structural steels: nonlinear isotropic/kinematic hardening material model and its calibration. J Struct Eng. 2021;147(4):04021031. doi:10.1061/(asce)st.1943-541x.0002964.
21. Liang G, Li Y, Liu Y, Yang J, Guo H. Residual mechanical property and resistance model for Q460 high-strength steel multi-staggered-hole plate with fatigue damage. Constr Build Mater. 2025;492:142875. doi:10.1016/j.conbuildmat.2025.142875.
22. Liu Y, Liu K, Wang W, Fan L, Li B, Yang T. Study on the inherent magnetism and its relationship with mechanical properties of structural round steel. Sci Rep. 2022;12(1):16078. doi:10.1038/s41598-022-20718-2.
23. Liu L, Bao S. Experimental research on the effect of cracks on metal magnetic memory signals. Eng Mech. 2024;41(5):247–56. (In Chinese).
24. Ma H, Zheng H, Zhang W, Tang Z, Lui EM. Experimental and numerical study of mechanical behavior of welded steel plate joints. Metals. 2020;10(10):1293. doi:10.3390/met10101293.
25. Lv L, Sun G, Yang W. Influence of axial compression ratio on hysteretic behavior of I-shaped steel tube bundle high-strength concrete composite shear wall. J Suzhou Univ Sci Technol Eng Technol Ed. 2023;36(1):8–14. (In Chinese).
26. Cao H, Wang G, Liu H. Research on seismic performance of corrugated web rigid structures. Rev Int Métodos Numér Cálc Diseño Ing. 2024;40(1):9. doi:10.23967/j.rimni.2024.03.001.
27. Zhu BL, Liu WC, Hou J, Guo YL. Simplified shear-resistant computational model of vertically corrugated steel plate shear wall embedded in frame structure. Structures. 2025;75:108817. doi:10.1016/j.istruc.2025.108817.
28. Lin HP, Chang SC, Chu C. Modal characteristics of planar multi-story frame structures. J Mech. 2016;32(5):501–14. doi:10.1017/jmech.2016.69.
29. Qi L, Xue J, Zhai L, Zhao X, Leon RT. Experimental and numerical studies on seismic performance of traditional style steel-concrete composite frame. Compos Struct. 2018;201:514–27. doi:10.1016/j.compstruct.2018.06.049.
30. Xu G, Zheng L, Bao Y. Shaking table substructure test of tuned liquid damper for controlling earthquake response of structure. Struct Control Health Monit. 2022;29(12):e3122. doi:10.1002/stc.3122.
31. Vasiljević R. Numerical methods and their application in dynamics of structures. Vojnoteh Glas. 2023;71(2):452–72. doi:10.5937/vojtehg71-42781.
32. Han M, Zhao MH, Du HK, Jiang JW. Study on structural dynamic response under near fault ground motion with different time-frequency characteristics. Acta Seismol Sin. 2022;44(5):911–9. (In Chinese). doi:10.11939/jass.20220135.
33. Feng ZJ, Wang YR, Cai J, Zhang C, Zhu JX, Meng YY. Dynamic response characteristics of large diameter variable section single pile under the coupling action of pile-splinter soil layer. J Vib Eng. 2025;38(1):162–71. (In Chinese). doi:10.16385/j.cnki.issn.1004-4523.2025.01.018.